The Boiling Crisis Phenomenon in Two-phase Flow

B. Sedler*
University of Stellenbosch

An analytic model of the flow boiling crisis in annular flow (at high vapour quality) and own experimental results of Freon 21 are presented in the paper. The model is based on the analysis of the film drying process on the channel wall, thus expressing the mass balance of both the film and the core by means of differential equations. The solution of these equations contains the parameters determined experimentally since theoretical predictions are not possible at this stage.

Nomenclature

C parameter in the mass transfer equations
c concentration of droplets in the flow core
D mass flux of deposition
d non-dimensional mass flux of deposition d = D/G, channel diameter
E mass flow of entrainment
e non-dimensional mass flux of entrainment e = E/G
G mass flux of the main flow
g non-dimensional mass flux of the main flow
K parameter in the mass transfer equations
k mass transfer coefficient
p pressure
r latent heat of vaporization
S non-dimensional constant $S = \frac{Yz_{cr}}{2x_{cr}}$
t non-dimensional parameter $t = x_{cr}\frac{z^+}{z_{cr}^+}$
V non-dimensional specific volume $V = \frac{v_L}{v_G}$
v specific volume
x steam quality
Y parameter
z longitudinal co-ordinate
z^+ non-dimensional longitudinal co-ordinate
q heat flux
q^+ non-dimensional heat flux

Greek symbols

ρ specific density
σ surface tension
μ dynamic viscosity
ν kinematic viscosity

Subscripts

c droplet in the core; core
E entrainment; equilibrium
D deposition
F film
G gas
j flow core
cr boiling crisis, critical state
L liquid
o beginning of the annular flow, channel diameter

Introduction

The boiling crisis phenomenon occurs in different technical devices, e.g. in nuclear reactors, steam generators and refrigeration evaporators. In the case of the high parameters equipment with two-phase vapour-liquid flow (boiling nuclear reactors, steam generators) the boiling crisis may result in serious damage due to the burn-out of the steam channels. In the low parameters steam generators, e.g. working on low-boiling media, the crisis diminishes the heat transfer intensity and is not desirable for technical reasons. Such generators are of increasing interest. Besides in refrigeration technology, they are used in utilizing the waste heat of chemical processes and will probably be applied in the new geothermal or solar plants with turbines working on low-boiling media.

Boiling is generally characterized by a high heat transfer coefficient, so that a large heat flux can be sustained at a fairly low temperature difference between the heat transfer surface and the boiling fluid. However, if attempts are made to increase the heat flux beyond a certain level, the nature of the boiling process changes radically and the heat transfer coefficient drops dramatically. This limiting heat flux is known as the "critical heat flux – CHF" or as "burn-out" [7, 10]. Numerous investigations performed in the last decade were concerned with the mechanism of the boiling crisis and the methods of its prediction.

Satisfactory solutions of this very complex problem have not yet been obtained. Practically no comprehensive analytic studies of the boiling crisis phenomenon exist, except for some simple models. As a substantial number of data does now exist, mostly for water, empirical or semi-emperical solutions [1, 15, 25], as well as a solution based on an annular flow model [6, 9-13, 26-29] were established, these solutions being applicable to any fluid.

Another criterion of dry-out as a limit of mist flow in upstream approach [18] can be very useful in establishing the scaling law for the modelling of the CHF in drop-annular flow.

A general review on recent work in this field is provided for example in [17] and [24]. In this paper an analytic model of the boiling crisis at high vapour quality and the author's investigations of that phenomenon are presented. The model employs the analysis of the film dry-out process on the wall which allows formulation of the differential equations of mass balance in the film and the core. The solution of these equations contains the parameters which are determined experimentally, since their theoretical prediction involves serious difficulties.

The theoretical model of the flow boiling crisis

The analytic model of flow boiling crisis in annular flow (at high vapour quality) is presented below. The model is based on the Harwell annular CHF model [26]. The Harwell model based on the film dry-out process involves a complex computer procedure, but gives fairly good results for water and other media, e.g. Freon 12, Fig. 1,2 [9]. In this paper the basis of an analytical model of the boiling crisis at high vapour quality and the author's investigations of that phenomenon are presented [20-24]. Let us consider the two-phase annular flow of mass flux G in a circular channel of internal diameter d_0. The liquid film

*Senior Lecturer
Department of Mechanical Engineering
University of Stellenbosch
7600 Stellenbosch

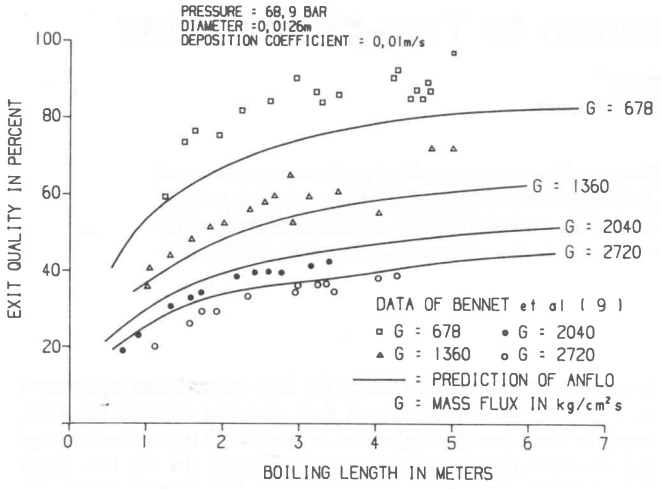

Figure 1 – Dryout in steam-water flow after [9]

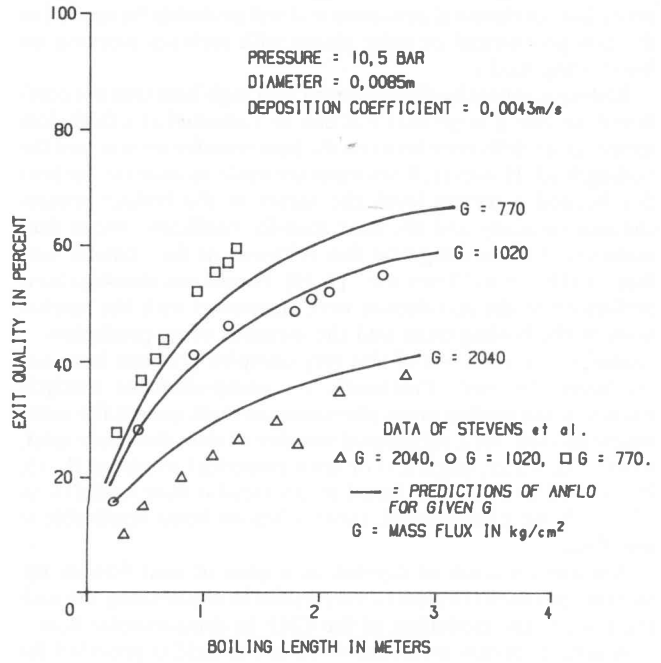

Figure 2 – Dryout in Freon-12 flow, after [9]

covers the channel wall, and the vapour with suspended droplets of liquid, flows in the core, Fig. 3. The beginning of the annular flow pattern is assumed to be known and from that point the mass balance starts. As a criterion of the CHF the film dry-out on the wall is assumed; however, recent investigations [19] suggest film breakdown into rivulets rather than its entire evaporation. For the sake of simplicity it is assumed that the crisis occurs at a film flow-rate equal to zero. This simplification was justified in [21, 22]. The mass flux of evaporation from the liquid film due to the wall heat flux q, is equal to q/r. This process is accompanied by the droplet entrainment from the film surface E and the droplet deposition onto the film surface D. The "flashing" terms [28] are not considered as secondary effects.

In accordance with the assumed model, the elementary mass changes of the film and the core are:

$$\frac{dg_F}{dz^+} = 4\,(d - e + q^+) \tag{1a}$$

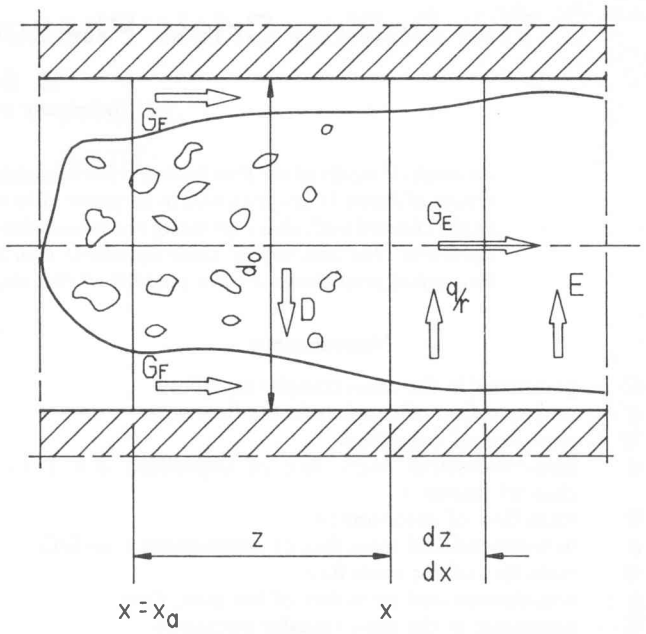

Figure 3 – A model of the annular flow with boiling

$$\frac{dg_E}{dz^+} = 4\,(-d + e) \tag{1b}$$

where

$$d = \frac{D}{G};\ e = \frac{E}{G};\ q^+ = \frac{q}{rg};\ z^+ = \frac{z}{d_o}$$

In order to solve the set of equations (1a, b) the fluxes d and e must be known. It was assumed

$$e = K.C.g_F \tag{2}$$

$$d = C.g_E \tag{3a}$$

where K and C are the parameters not exactly defined at the moment. This assumption differs from the Harwell model, but according to [2, 3, 5, 8, 14, 29], experiments show that the dimensionless deposition coefficient is a function of the concentration of entrained droplets and the rate of entrainment is proportional to the liquid film flowrate and to the gas velocity, Fig. (4, 5). These relations are also expressed by eqs. (2, 3a).

According to [26] the deposition mass flux rate d may be expressed by

$$d = \frac{k.c_j}{G} \tag{3b}$$

where k is the mass transfer coefficient and c_j signifies the concentration of liquid within the core and may be determined after [13], as

$$c_j = \frac{1 - x_j}{(1 - x_j)\,v_L + x_j\,v_g} \tag{4}$$

Steam quality within the flow core is defined as follows:

$$x_j = \frac{G_G}{G - G_F} = \frac{1 - g_E - g_F}{1 - g_F} \tag{5}$$

The general formula describing the mass transfer coefficient k is given in [21] as

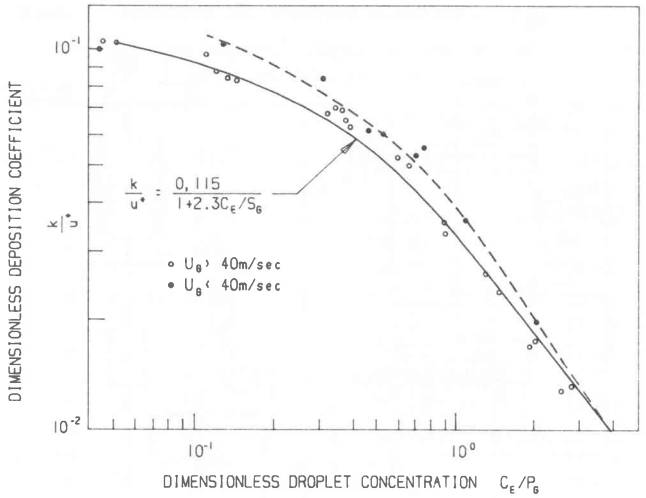

Figure 4 – Correlation of deposition coefficient by dimensionless relaxation time, after [3]

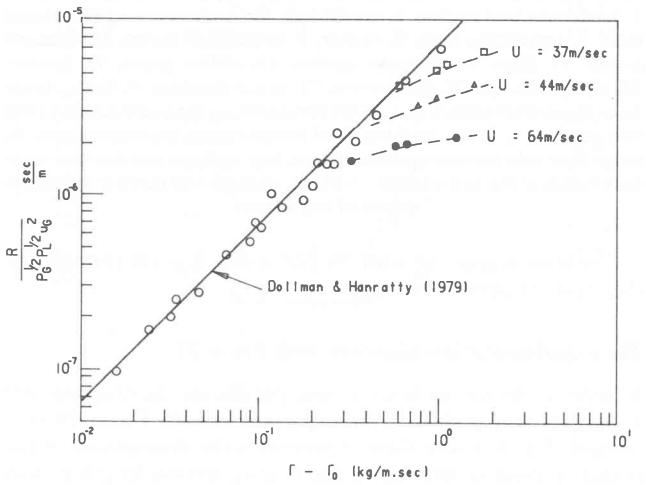

Figure 5 – Correlation of the rate of entrainment as a function of the Liquid flowrate per unit perimeter, after [3]

$$k = C_k \frac{G^n}{d_o^m} (1 - g_F - g_E)^n \tag{6}$$

where C_k is a function of the fluid properties and the two-phase characteristics (v_G, μ_G, T, ρ_c, ν_c, d_c ...) and m, n are not exactly known exponents*.

Combining equations (2), (3a, b), (4) and (6) one finds

$$d = C_k' \frac{g_E(1 - g_F - g_E)^n}{g_E v_L + (1 + g_F - g_E) v_G} \tag{7}$$

$$e = KC'_k \frac{g_F (1 - g_F - g_E)^n}{g_E v_L + (1 + g_F - g_E) v_G} \tag{8}$$

where $$C_k' = C_k \frac{G^n - 1}{d_o^m} \tag{9}$$

Then from equation (1a, b), (7) and (8) a set of nonlinear differential equations describing the dimensionless mass fluxes within the film and the core is obtained

*For small droplets $d_o \leq 0,1$ μm, n = 0,8, m = 0,2, [21].

$$\frac{dg_F}{dz^+} = 4 \left(C_k' \frac{g_E (1 - g_F - g_E)^n}{g_E v_L + (1 + g_E - g_F) v_G} - K C_k' \frac{g_F(1 - g_F - g_E)^n}{g_e v_L + (1 - g_E - g_F) v_G} - q^+\right) \tag{10a}$$

$$\frac{dg_E}{dz^+} = 4 \left(-C_k' \frac{g_E (1 - g_F - g_E)^n}{g_E v_L + (1 + g_E - g_F) v_G} + K C_k' \frac{g_F(1 - g_F - g_E)^n}{g_E v_L + (1 - g_E - g_F) v_G}\right) \tag{10b}$$

Rearranging equations (10a, b) one obtains the first-order nonlinear differential equation for the film mass flux

$$\frac{dg_F}{dt} = S \frac{(1 - g_F - g_E)^n (g_E - K.g_F)}{g_E V + (1 - g_E - g_F)} - 1 \tag{11}$$

where $$t = x_{cr} \frac{z^+}{z_{cr}^+} \tag{12}$$

$$S = \frac{4z_{cr}^+ C_k'}{x_{cr} v_G} = \frac{Y z_{cr}}{2 x_{cr}} \tag{13}$$

$$V = \frac{v_L}{v_G} \tag{14}$$

and $$q^+ = \frac{x_{cr} - x_o}{4z_{cr}^+} \simeq \frac{x_{cr}}{4z_{cr}} \tag{15}$$

According to Hewitt [13], and Whalley et al [26], it was recognised that the annular flow pattern exists at a steam quality equal to 0,01 and if the share of the film flow is about 0,01 of the total mass flow-rate of the liquid phase. However the most recent results [9], show that for high-pressure water-steam flow the annular flow conditions occur at $x_o = 0,05$. For the higher steam qualities at the onset of annular flow, equation (11) takes the following form:

$$\frac{dg}{dt^*} = S^* \frac{(1 - g_F - g_E^{\sim})^n (g_E - K g_F)}{g_E V + (1 - g_E - g_F)} - 1 \tag{11*}$$

where

$$t^* = (x_{cr} - x_o) \frac{z^+}{z_{cr}^+} \tag{12*}$$

$$S^* = \frac{4z_{cr}^+ C_k}{(x_{cr} - x_o) v_G} = \frac{Yz_{cr}}{2(x_{cr} - x_o)} \tag{13*}$$

$$q^+ = \frac{x_{cr} - x_o}{4z_{cr}^+} \tag{15*}$$

and other quantities remain unchanged.

Equation (11) or (11*) cannot be solved analytically and, hence, a numerical method was used. As a result the function of the critical steam quality x_{cr} vs the non-dimensional co-ordinate Yz_{cr} for selected values of K, n and V was obtained. The results are shown in Fig. 6. For the sake of comparison the results of the analytic solution of the simplified form of equation (11) with the assumption of n = 1 and V $\cong$ 0 are presented in Fig. 6. The above simplifications allow direct determination of the steam quality in the cross section of crisis (where the film disappears) as a function of non-dimensional co-ordinate of boiling Yz_{cr} (or $Yz_{cr}^{\cdot}$).

Figure 6 – The generalized function X_{cr} ($Y2_{cr}$) predicted numerically for n = 0,8, V = 0,5 vs the simplified analytic solution for n = 1, V = 0 after equation (16)

From equation (11)

$$x_{cr} = \frac{0{,}99\, e_A - (0{,}98 - 0{,}01K)}{\frac{K}{A}(e_A - 1) + e_A} \cong \frac{1}{\frac{K}{A} + \frac{e_A}{e_A - 1}} \qquad (16)$$

where $A = \frac{1 + K}{2} Y z_{cr}$

For large values of K (> 20) equation (16) takes a simpler form

$$x_{cr} = \frac{1}{1 + 2/Y z_{cr}} \qquad (16a)$$

which is similar to that determined experimentally by Silvestri (after [4]). From equation (11*)

$$x_{cr} = \frac{(1 - g_{Fcr}(1 + K))e_{A^+} + (x_o + g_{Fo}(1 + K) - 1) + K/A^+ X_o^+ (e_{A^+} - 1)}{K/A^+ (e_{A^+} - 1) + e_{A^+}} \qquad (16^*)$$

$$A^+ = \frac{Y z_{cr}^+ (1 + K)}{2}$$

The influence of the quantities g_{Fo}, x_o and g_{Fcr}, is shown in Fig. 7. It is seen from Fig. 6 that the analytic solution of the simplified form of equation (11) given by equation (16) is similar to the numerical solution of the exact equation (11). The further analysis is continued with the simplified model described by equation (16).

The parameter Y has a dimension $[m^{-1}]$ and, as it follows from the analysis performed in [21], is a function of the typical parameters influencing the crisis: mass flux G, channel diameter d_o, viscosity of the gas phase μ_G, specific volume of the gas phase v_G etc.

The analytic determination of Y for given crisis conditions is rather difficult and it seems most reasonable to correlate that parameter on an experimental basis.

Figure 7 – Analytic solution X_{cr}^+ vs $Y2_{cr}^+$ after equation (16*); n = 1, V = 0

Figure 8 – Layout of the experimental apparatus for the boiling crisis investigations. 1. vertical test section, 2. by-pass, 3. safety-valve, 4. horizontal test section, 5. condenser, 6. condensate measurement tank, 7. equalizing tank, 8. cooler, 9. circulation pump, 10. vacuum pump, 11. filter, 12. by-pass cooler, 13. orifice plate, 14. heater, 15. main tank, 16. DC generators, 17. crisis detector, P_1 to P_{111} pressure measurements, t_1 to t_9 wall temperature measurements of the test section, t_9 to t_{111} working fluid temperature measurements, G, mass flow rate measurements, $\triangle$Uop, Iop, voltage and current measurements of the test section, $\triangle$Up, Ip, voltage and current measurements of the heater.

The same is applicable for the parameter K in the formula for the mass transfer of entrainment rate e.

The experimental investigations with Freon 21

In order to determine both of these parameters an experimental apparatus was built and the experiments with Freon 21 performed, Fig. 8. From these experiments the dependence of the critical vapour quality x_{cr} vs the boiling section length z_{cr} was established. The length of the boiling section was determined from the heat balance with an additional assumption of x_o = 0,01 at the beginning of the annular flow pattern. Subsequently, the curves predicted from the simplified analytic model [eq. (16)] were fitted to the experimental points using the least squares technique. Therefore, as a result of optimisation computations based on equation (16) the best values of the parameters K and Y were obtained. It was established that the parameter K for Freon 21 varies between 16 and 26 and may be assumed to be a constant equal to 20. Such an assumption slightly affects the analytic curve (16) and substantially simplifies further considerations.

It was mentioned before that the parameter Y is the following function

$$Y = Y(G, p, d_o, \ldots) \qquad (17)$$

Moreover, this parameter may be affected by the other properties, not expressed in equation (17), but influencing deposition or the entrainment process, e.g. surface tension σ. Dimensional analysis of Y provides the non-dimensional number Yd_o dependant on the two-phase flow criterial numbers. The following expression for Yd_o is proposed.

$$Yd_o = A \left(\frac{G\, d_o}{\mu_G}\right)^b \left(\frac{p_L\, \sigma\, d_o}{\mu_G^2}\right)^{b_1} f\left(\frac{p}{p_{cr}}\right) \qquad (18)$$

The constants A, b and b_1 and the form of function $f(p/p_{cr})$

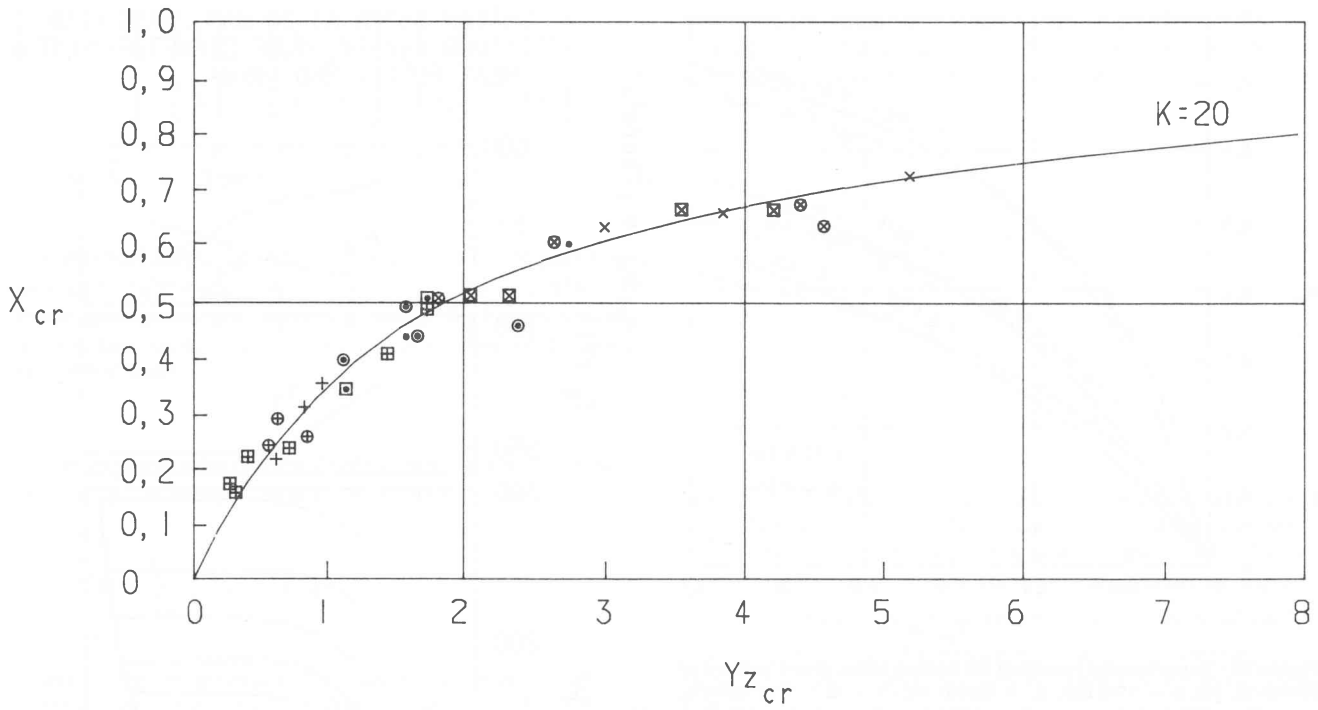

Figure 9 – Critical vapour quality X_{cr} vs non-dimensional critical boiling length YZ_{cr} after eqns (16) and (20) in comparison with the experimental data for Freon-21 (d_o = 0,008 m, p = 5,5, 10,6, 15,0 bar)

were determined from the experiments with Freon 21 so that the following formula for Y d_o was obtained.

$$(Y\ d_o)_{R-21} = 1{,}27 \times 10^6 \left(\frac{G\ d_o}{\mu_G}\right)^{-1{,}40} \left(1 - 1{,}9\ \frac{p}{p_{cr}}\right) \qquad (19)$$

In the experiments with Freon 21 the mass flux G and the pressure were variable and the tube diameter d_o was constant.

The critical vapour quality x_{cr} as predicted by equation (16) and (19) is compared to experimental results in figure 9. It follows that 74% of the experimental points lie within the error of plus minus 10% and all of them within plus minus 25% error.

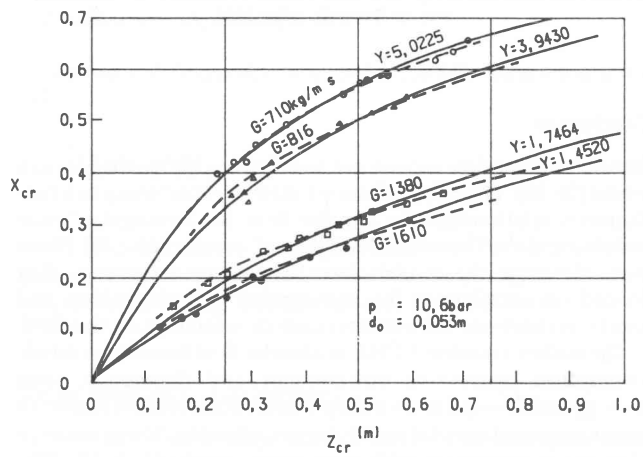

Figure 10 – Experimental results of the boiling crisis investigations of Freon-12, [4], p = 10,6 bar, d_o = 0,0053 m: ○ – G = 710 kg/m²s, △ – G = 815 kg/m²s, □ – G = 1380 kg/m²s, ● – G = 1610 kg/m²s, (...) after [4], (–) eqn (16)

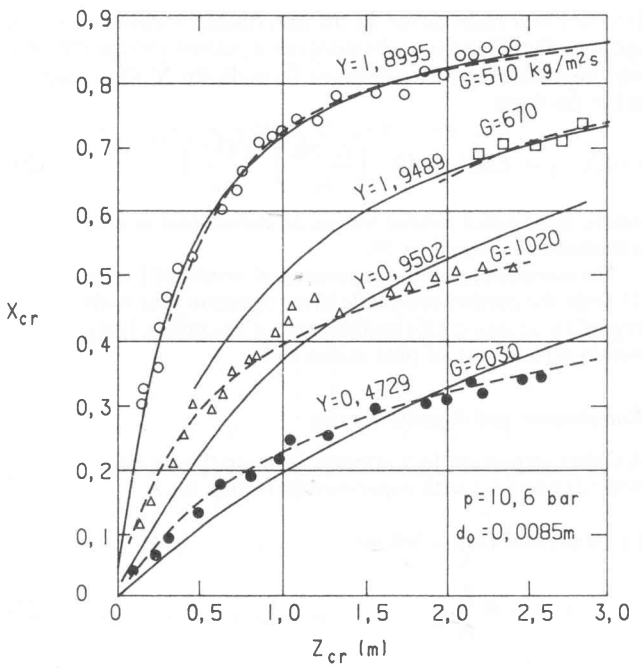

Figure 11 – Experimental results of the boiling crisis investigations of Freon-12, [4], p = 10,6 bar, d_o = 0,0085 m: ○ – G = 510 kg/m²s, □ – G = 670 kg/m²s, △ – G = 1020 kg/m²s, ● – G = 2030 kg/m²s; (...) after [4], (–) eqn (16)

The comparison of the experimental results for Freon 21 and Freon 12

For the sake of comparison the predictions after the model described here were carried out for the experiments with Freon 12 performed by Stevens, (after [4]). The results, shown in Figs. 10-12 are in very good agreement with the experiments, particu-

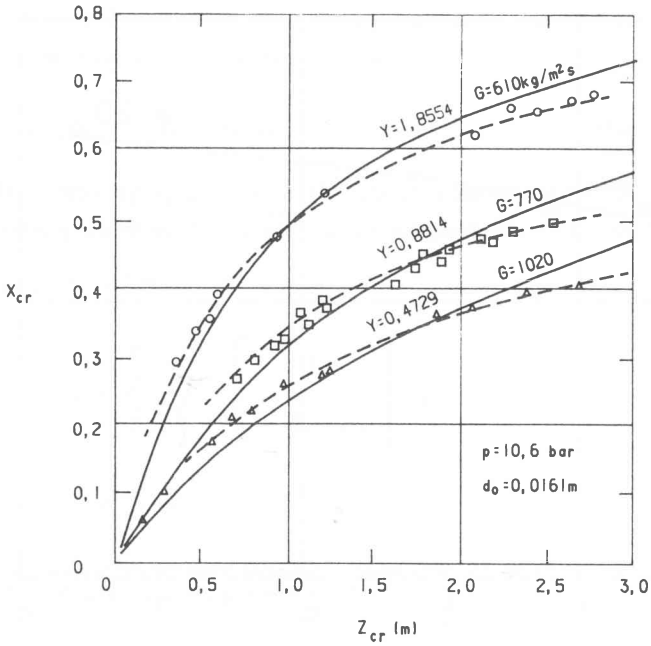

Figure 12 – Experimental results of the boiling crisis investigations of Freon-12, [4], p = 10,6 bar, d_o = 0,0161 m: ○ – G = 510 kg/m²s, □ – G = 770 kg/m²s, △ – G = 1020 kg/m²s; (...) after [4], (–) eqn (16)

larly at lower mass fluxes. In the experiments mentioned above the mass flux G and the tube diameter d_o varied and the pressure was kept constant. The relevant formula for Y for Freon 12 takes the form.

$$(Yd_o)_{R-12} = 1{,}805 \times 10^{-3} \left(\frac{\rho_L \sigma d_o}{\mu_G^2}\right)^{1.17} \left(\frac{Gd_o}{\mu_G}\right)^{-1.60} \qquad (20)$$

where K assumes similar values as before and is also assumed to be equal to 20.

The comparison of the experimental results of Freon 12 with the predictions made after equation (16) with regard to equation (20) shows most of the points lying within error limits of plus minus 15%.

Entrainment and deposition rates

Another important fact appears from analysing equation (2) and (3a) with experimental results for K.

From (2) and (3a) it follows

$$e = k.d.\frac{g_F}{g_E} \qquad (21)$$

where K can be assumed as about 20 and $g_{Fo}/g_{Eo} \simeq 0{,}01$ (according to Hewitt [13]).

then

$$e_o \cong 0{,}20\ d_o \qquad (21a)$$

which is a local value at the beginning of annular flow and corresponds fairly well with the last results of the calculation of e and d rates, Fig. 13, [29]. It can also be seen that the local entrainment to the deposition rate becomes less in the axial direction toward CHF point which is in agreement with the assumed model and was previously indicated by Hewitt, [13].

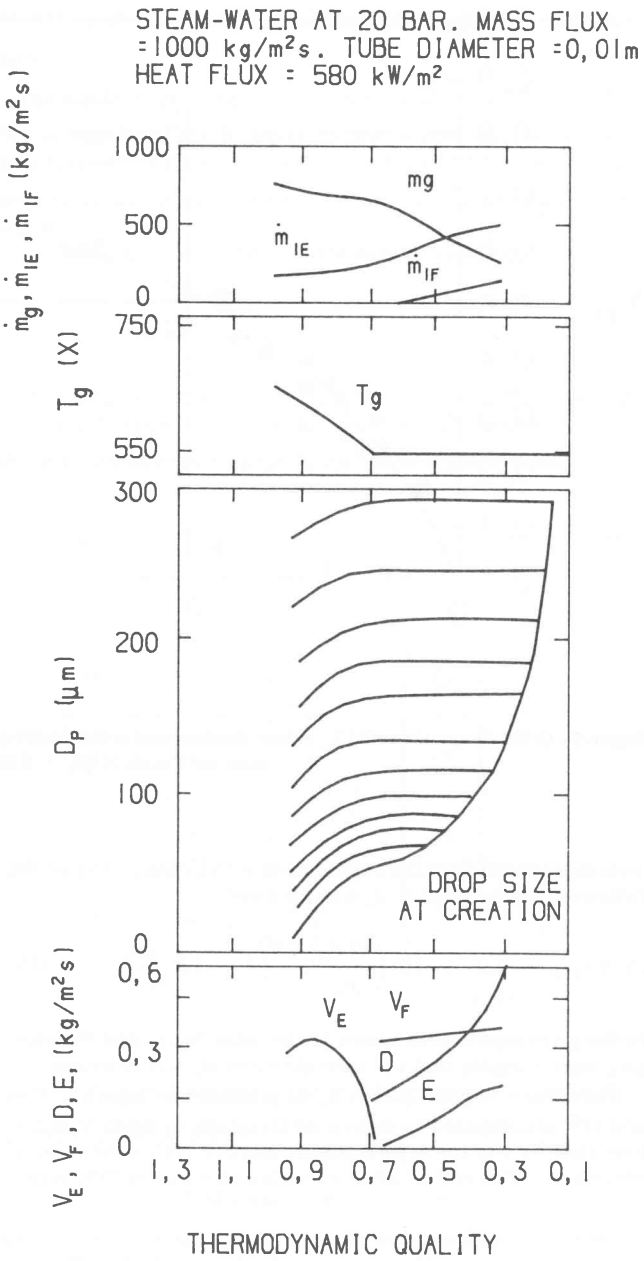

Figure 13 – Calculations of local parameters in evaporating flow with dryout and subsequent post-dryout region (UKAEA Harwell/University of Oxford), after [29]

Conclusions

Present annular flow models are based primarily on the Harwell model [26-29]. The calculations are made by combining two fundamental relationships for annular flow: the "triangular" relationship and the "interfacial roughness" correlation, [10]. However, although the models have been very successful, they depend on correlations for entrainment rate, deposition and interfacial friction. The current research is focused on this field.

The author's model of CHF in annular flow based on a simple assumption concerning entrainment and deposition rates ($e \sim g_F$ and $d \sim g_E$) gives a simple analytical solution similar to recent empirical correlations (Silvestri, after [4]). These assumptions are in agreement with most recent results [3, 5, 12, 29].

The correlations established for K and Y [equations (19), (20)] are, presently specific for each medium.

It is hoped that further theoretical and experimental research

will result in a more precise identification and determination of these parameters and, possibly, a general relationship valid for different media will be produced.

References

1. Ahmad, S. Y., "Fluid-to-fluid modelling of critical heat flux: a compensated distortion model" *Int. J. Heat Mass Transfer,* Vol. 16, pp. 641-661, 1973.
2. Andreussi, P., Azzopardi, B. J., "Droplet deposition and interchange in annular two-phase flow", *Int. J. Multiphase Flow,* Vol. 9, No. 6, pp. 681-695, 1983.
3. Andreussi, P., "Droplet transfer in two-phase annual flow", *Int. J. Multiphase Flow,* Vol. 9, No. 6, pp. 697-713, 1983.
4. Cumo, M., Maciuca, C., Moronesi, M., Palazi, G., "A burn-out correlation to scale water with Freon", *European Two-Phase Flow Group Meeting,* Harwell (1974).
5. Dallman, J. C. Laurinat, J. E., Hanratty, T. J., "Entrainment for horizontal annular gas-liquid flow", *Int. J. Multiphase Flow,* Vol. 10, No. 6, pp. 677-690, 1984.
6. Dobran, F., "Hydrodynamic and heat transfer analysis of two-phase annular flow with a new liquid film model of turbulence", *Int. J. Heat Mass Transfer,* Vol. 26, No. 8, pp. 119-1171, 1983.
7. France, D. M., Chiang, T., Carlson, R. D., Priemer, R., "Experimental evidence supporting two-mechanism critical heat flux", *Int. J. Heat Mass Transfer,* Vol. 25, No. 5, pp. 691-698, 1982.
8. Ganic, .E. N., Mastanaiah, K., "Investigation of droplet deposition from a turbulent gas stream", *Int. J. Multiphase Flow,* Vol. 7, pp. 401-422, 1981.
9. Grover, R. B., "Two dimensional modelling of annular two-phase flow", *Heat Transfer 1982,* Proc. of the Seventh Int. Heat Transfer Conf., München, (1982), TF 17.
10. Hewitt, G. F., "Burnout", Stanford Univ. Course, Heat Transfer with Phase Change, August 15-19 (1983).
11. Hewitt, G. F., "Burnout", *Two-Phase Flow and Heat Transfer in the Power and Process Industries,* A. E. Bergles, J. G. Collier, J. M. Delhave, G. F. Hewitt, F. Mayinger, Hemisph. Publ., Corp., 1981.
12. Hewitt, G. F., "Two-phase flow studies in the United Kingdom", *Int. J. Multiphase Flow,* Vol. 9, No. 6, pp. 715-749, 1983.
13. Hewitt, G. F., "Mechanisms of Burnout", *Two-phase Flow and Heat Transfer,* D. Butterworth and G. F. Hewitt, Oxord University Press, 1977.
14. Ishii, M., Mishima, K., "Liquid transfer and entrainment correlation for droplet-annular flow", *Heat Transfer 1982,* Proc. of the Seventh Int. Heat Transfer Conf., München (1982), TF 20.
15. Katto, Y., Ohno, H., "An improved version of the generalized correlation of critical heat flux for the forced convective boiling in uniformly heated vertical tubes", *Int. J. Heat Mass Transfer,* Vol. 27, No. 9, pp. 1641-1648, 1984.
16. Katto, Y., "Prediction of critical heat flux for annular flow in tubes taking into account the critical liquid film thickness concept", *Int. J. Heat Mass Transfer,* Vol. 27, No. 6, pp. 883-891 (1984).
17. Katto, Y., "Critical heat flux", *Adv. in Heat Transfer,* Vol. 17, ed. by J. P. Hartnett and T. F. Irvine, Jr., Academic Press, Inc. (1985).
18. Madejski, J., "A new criterion of dry-out in two-phase flow", *Int. J. heat Mass Transfer,* Vol. 24, No. 10, pp. 1657-1665, 1981.
19. Mikielewicz, J., Moszynski, J., "Minimum thickness of a liquid film flowing vertically down a solid surface", *Int. J. heat Mass Transfer,* Vol. 19, pp. 771-776, 1976.
20. Sedler, B., Mikielewicz, J., "A simplified model of the boiling crisis", *Int. J. heat Mass Transfer,* Vol. 24, pp. 431-438, 1981.
21. Sedler, B., "An analysis of the flow-boiling crises in low-boiling media on an example of Freon 21", (in Polish), Ph.D. Thesis, Institute of Fluid Flow Machines, Gdansk, Poland (1977).
22. Sedler, B., Mikielewicz, J., "A simplified analytical model of the flow boiling crisis", (in Polish), *Transaction of the Institute of Fluid Flow Machines,* No. 76, PWN Warsaw-Poznań (1978).
23. Sedler, B., "Analysis of boiling crises in a flow of low-boiling media", *Trans. of the Institute of Fluid Flow Machines,* No. 80, PWN Warsaw-Poznań (1981). Presented on Symp. – Technishe Hochschule Karlsruhe, Inst. der Verfahrens Tech., Feb. 1980.
24. Sedler, B., "Boiling crisis phenomenon in two-phase Flow", Int. Report – Dep. of Mech. Eng., University of Stellenbosch, R.S.A. (1985).
25. Shah, M. M., "A general correlation for critical heat flux in annuli", *Int. J. Heat Mass Transfer,* Vol. 23, pp. 225-234, 1980.
26. Whalley, P. B., Hutchinson, P., Hewitt, G. F., "The calculation of critical heat flux in forced convection boiling", *Fifth Int. Heat Transfer Conf.,* Japan (1974).
27. Whalley, P. B., Hutchinson, P., James, P. W., "The calculation of critical heat flux in complex situations using an annular flow model", *Sixth International Heat Transfer Confer.,* Toronto, (1978).
28. Whalley, P. B., Lyons, A. J., Swinnerton, D., "Transient critical heat flux in flow boiling", *First U.K. National Confer. on Heat Transfer (1984),* The Inst. of Chem. Eng. Symp. Ser. No. 86, pp. 805-816.
29. Whalley, P. B., Azzopardi, B. J., Hewitt, G. F., Owen R. G., "A physical model for two-phase flows with thermodynamic and hydrodynamic non-equilibrium", *Heat Transfer, 1982,* Proc. of the Seventh Int. Heat Transfer Conf. München, (1982), CS 29.
30. Wilkes, N. S., Azzopardi, B. J., Thomspon, C. P., "Wave coalescence and entrainment in vertical annular two-phase flow", *Int. J. Mutiphase flow,* Vol. 9, pp. 383-398, 1983.

RESEARCH NOTES

Crack initiation sites, crack shape development and crack growth rates observed in the fatigue testing of fillet welded joints

C. A. Boothroyd* and G. G. Garrett**
University of Witwatersrand, Johannesburg

Introduction

Cracking was observed in a small number of all-welded steel fans, used extensively in the power generation industry for the supply of air to, and extraction of gases from, boilers in coal-fired power stations, and for ventilation purposes in mines. These fans operate at around 700 rpm, and in a year of continuous operation, can experience in excess of 300 million cycles. The cracking was shown to initiate by fatigue, typically from balance pad welds, and in one particular instance [1] led to catastrophic failure. Initially, the balance pads were regularly stitch welded in position, but it was thought that this gave rise to a large stress concentration at the weld root. The procedure was therefore revised, such that the corners of the balance pad were rounded, a local pre-heat of 150 °C was applied, and the weld was made continuously around the attachment.

However, the Welding Institute Design Rules [2] for welded steel joints indicate that both these weld details would be classified as "G" type joints and could therefore be expected to have the same fatigue strength. Accordingly, a test programme was initiated in order that the fatigue strength of the two details could be experimentally determined. Specimens simulating both types of welding were supplied for the initial test work [3].

The results of these tests indicated that the revised procedure for balance pad welding would only have an improved fatigue strength if there were no undercut defects at the weld toe. In the presence of weld toe undercut, the endurance limit of the continuous welds would be the same (50 MPa) as the stitch type welding. (The deleterious effect of weld toe defects on fatigue strength was demonstrated as early as 1960 [4]; more recently, a stress concentration factor of up to 27 was calculated for an undercut defect at the toe of a non-load-carrying fillet weld [5]).

As described in a companion paper to this [6], continuously welded specimens that had been dressed, either by grinding or by peening, were supplied for testing. The results of these tests clearly demonstrated the advantages of using these cost-effective mechanical dressing techniques. It was further observed that, if the dressing had been carried out correctly, the crack initiation site was removed from the weld toe to the weld root.

This experimental test programme was therefore aimed at establishing the 10 million cycle endurance limit of non-load-carrying fillet welds, and evaluating the effects of weld procedure and post-weld dressing techniques on this endurance limit. (The 10 million cycle endurance limit is defined as the highest stress range at which crack initiation did not occur for a given set of specimens.) As outlined above, it was essential to complement the results of the endurance limit testing with a macro-fractographic examination of the specimens. In the initial series of tests this indicated the necessity for post-weld mechanical dressing so that the preferential crack initiation sites at the weld toe would be removed to the weld root and in the tests on the ground and peened specimens, determination of the crack initiation site indicated whether or not this dressing had been effectively carried out.

Additionally, in order to evaluate the effect of the weld on the initiation and subsequent growth of a fatigue crack in these welded details, the crack tip stress intensity factor had to be calculated. The alternating stress intensity was then plotted against the rate of crack propagation in the conventional log-log form and compared to data obtained from the literature for similar tests. However, in order to evaluate the crack tip stress intensity and the crack propagation rate, it was necessary to either monitor the crack depth and shape throughout the tests, or to mark the crack front at various stages during the tests.

Experimental

All specimens were tested under four point bending conditions, since this simulated the operating conditions more accurately than direct tension loading. A 100 kN Amsler Vibrophore fitted with a Howden load controller was used for all tests, and starting frequencies of between 120 and 140 Hertz were achieved.

Following the catastrophic failure of a fan during service [1], an extensive series of long term strain gauge tests were carried out on a operating fan. These results [7] indicated that the mean service stress was 150 MPa, and the cyclic stress range under normal operating conditions was generally below 20 MPa, but could, in certain circumstances, exceed 30 MPa by a small amount. (These fans are in fact designed such that the only appreciable dynamic stresses that occur are those experienced during start-stop cycling).

Accordingly, each specimen was subjected to 50 000 start-stop cycles, with a stress range of 150 MPa, about a mean stress of approximately 75 MPa. These load cycles are intended to simulate the start-stop cycling experienced by the fans during dynamic balancing, as well as the other start-stop cycles that may be imposed on the fan during operation. Although it has been pointed out by the manufacturers that this number of start-stop cycles is well in excess of that experienced by a fan in typical service, there were no instances of crack initiation in any of the thirty eight specimens due to this initial loading sequence.

The mean stress was then increased to 150 MPa, and the stress range decreased to 60 MPa (40 MPa in the case of the stitch welded specimens), and the Amsler Vibrophore was set to run for 10 million loading cycles (or approximately 22 hours of continuous testing). In the event of any fatigue crack initiation, the specimen compliance increases, thereby decreasing the test frequency and the machine is stopped automatically. If crack initiation did not occur within this first period of 10 million loading cycles the stress range was increased by 10 MPa; this incremental increase in stress range was repeated every 10 million cycles until crack initiation was observed.

In addition to using the frequency monitoring module in the Howden load controller, crack initiation (and subsequent propagation) was monitored using a direct current potential drop

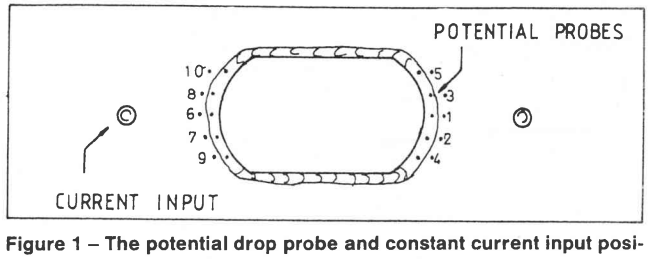

Figure 1 – The potential drop probe and constant current input positions on the test samples

*Metallurgist, SASTECH (SASOL Technology) Pty Ltd., Secunda.
**Chief Director, The National Institute for Materials Research (NIMR) at the CSIR, Pretoria.
(Both formerly with Department of Metallurgy and Materials Engineering, University of the Witwatersrand, Johannesburg).

(DCPD) system comprising a Gould constant current supply and a high resolution Fluke digital voltmeter. The potential drop was measured by spot welding pairs of Nichrome wires on either side of the expected crack initiation sites; the current leads were mechanically attached to the specimen remote from the weld (see figure 1).

In order to correlate the potential drop and frequency changes with crack advancement, the crack front was marked at intervals during the propagation. Initially this was carried out by heat-tinting (10 minutes at 500 °C), which resulted in various temper-colours on the fracture surface. However it was found that a particular specimen could only be heat-tinted at most four times, otherwise it was found difficult to distinguish the early crack shapes. Specimens were therefore subjected to load changes during the propagation stage, this giving characteristic "beach marks" on the fracture surface. In order to produce a clear beachmark, it is necessary to increase or decrease the stress range significantly, but maintain a constant maximum stress. Such a change in the loading conditions inevitably gave rise to a change in the operating frequency of the system; this complicated the correlation between frequency change and crack depth somewhat. (Obviously, if beach marks are to be produced by reducing the stress range, it is necessary to monitor the p.d. to ensure that some crack extension has occurred).

In the case of the dressed welds, it was seen that the crack initiation site was removed from the weld toe to the weld root, i.e. the crack initiation became subsurface. Furthermore, the crack propagation occurred on different fronts, only establishing the semi-elliptical equilibrium crack shape across these separate fronts after some considerable crack extension had occurred. Accordingly, the tests on the ground and peened welds were terminated at different stages (for example, one after 10 million cycles after initiation had occurred, one after 2 million cycles after initiation, and one immediately after initiation). Thus the fatigue crack front could be seen at the different stages, and the typical crack propagation path was established.

Results

Preferential crack initiation sites

Crack growth generally occurred on both sides of the stitch welded attachment, and initiation typically occurred at the root of the weld, at the corner of the balance pad, as shown in figure 2(a). However, there were some instances of crack initiation from the weld toe due to undercutting, as shown in figure 2(b). In the cases of weld root initiation, the preferred crack path through the weld metal was inclined at an angle towards the centre of the attachment, but as the cracks grew into the main load carrying plate, the growth became normal to the plate surface. This growth pattern has been noted elsewhere [5].

In the undressed continuously welded specimens, initiation occurred at the weld toe in all cases, and cracking only occurred on one side of the attachment. It was seen that a high initiation stress range (100 MPa or greater) was required in the absence of any undercut at the weld toe. The fracture surfaces of these specimens showed multiple initiation points at the weld toe, as shown in figure 3(a). Such "ratchet markings" are indicative of a relatively low stress concentration, all the way around the weld, as opposed to a very high but localised stress concentration at an undercut defect. The fracture surfaces of the specimens that recorded low endurance limits (less than 80 MPa) indicated that initiation had occurred at an undercut defect at the weld toe, as shown in figure 3(b).

In the ground and peened specimens, initiation typically occurred at the weld root, as shown in figure 4(a). However, if the weld had been insufficiently dressed, initiation could still occur

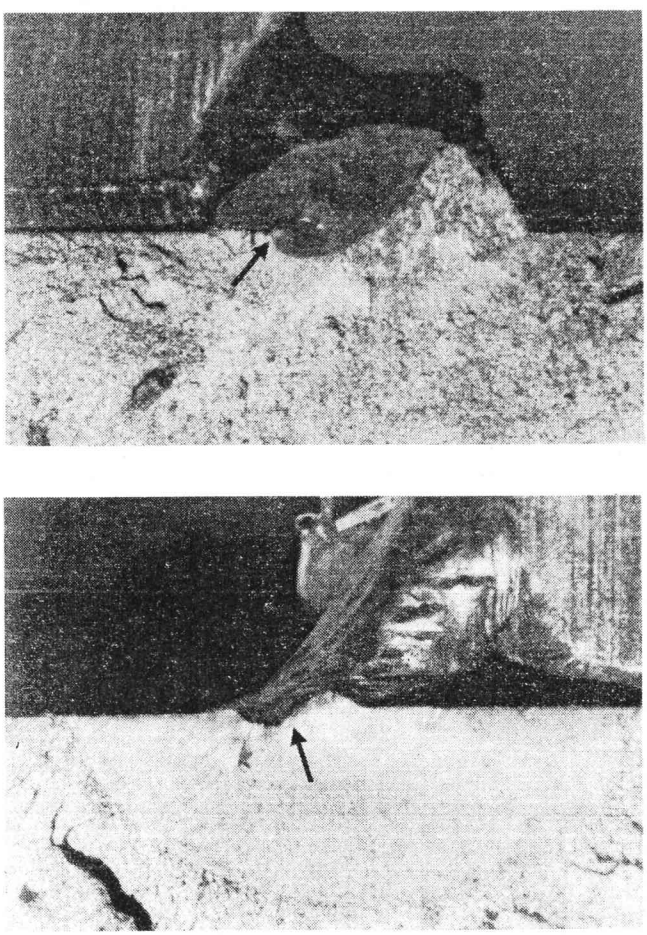

(a)

(b)

Figure 2 – Crack initiation from (a) the weld root and (b) the weld toe in the stitch welded samples, magnification 5 ×

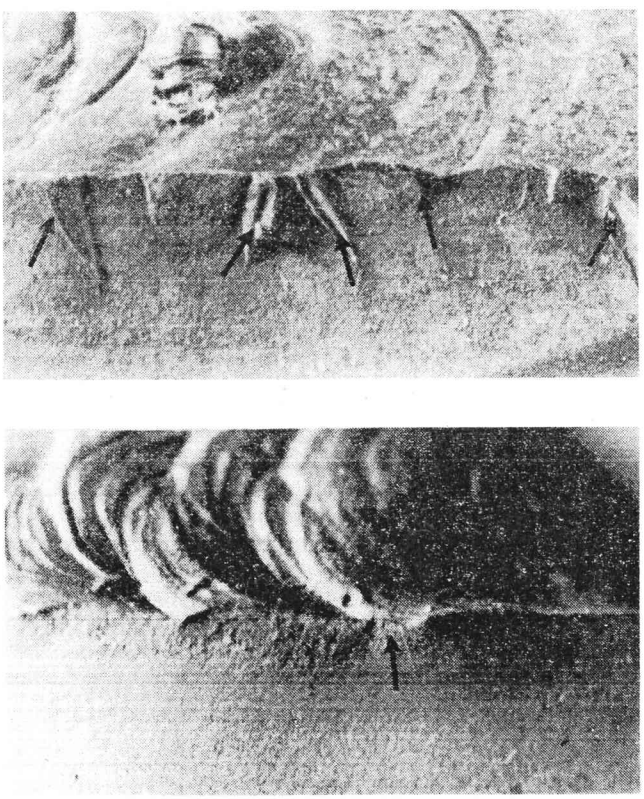

(a)

(b)

Figure 3 – Crack initiation in the continuous welds from (a) multiple points along the weld toe and (b) from an undercut defect, magnification 5 ×

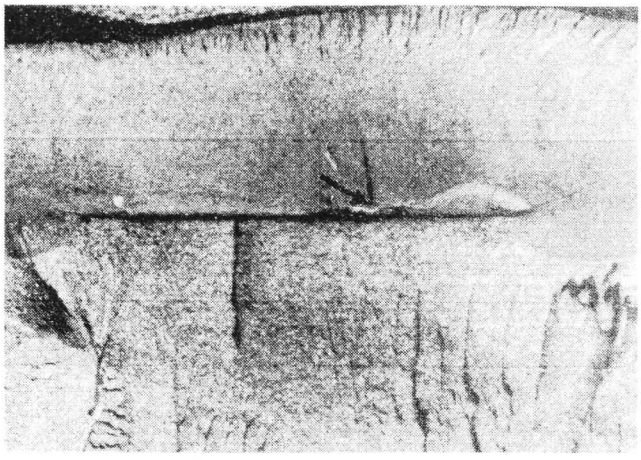

(a)

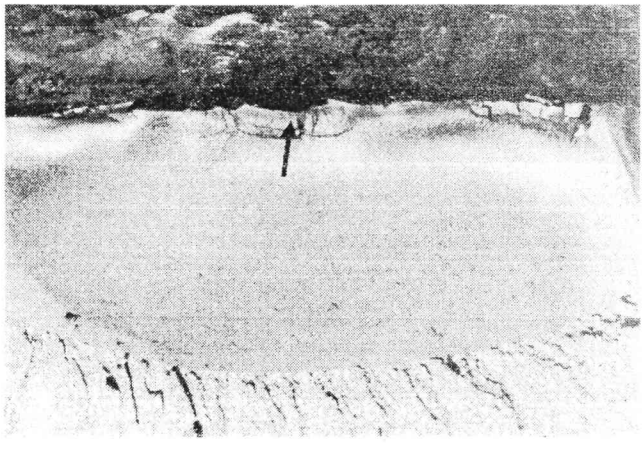

(b)

Figure 4 – Crack initiation from (a) the weld root and (b) the weld toe in the dressed specimens, magnification 4 ×

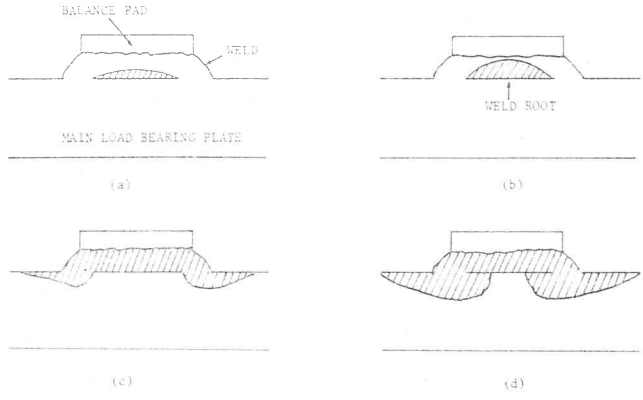

Figure 5 – Schematic representation of the stages in crack propagation in the ground and peened specimens

(a) initiation from weld root,
(b) propagation upwards to the surface of the weld,
(c) propagation downwards from the side welds and
(d) propagation downwards and across the main load bearing plate (not to scale)

from weld toe defects, as shown in figure 4(b). In some instances, fatigue crack initiation occurred at the edge of the main load-carrying plate remote from the weld. (The specimens had been flame cut, and the sides were not machined before testing). It has been shown [8] that micro-cracking can result from even high quality gas cutting; the effectiveness of the mechanical dressing procedures was most clearly illustrated by such cases of initiation remote from the weld.

Crack shape development

The results detailed in this section refer only to the continuous welds that were not dressed by grinding or peening. This is due to the fact that the dressed welds showed multiple crack propagation paths, and subsurface initiation. This latter point complicated the p.d. work, since, as the probe pairs have to straddle the crack, the spacing had to be much greater for these welds; consequently, the p.d. indications were less accurate. In addition the weld root initiation would greatly complicate the calculation of the cyclic stress intensity, even if the change in crack depths and lengths across these multiple crack fronts could have been evaluated. Thus these dressed specimens were not subjected to any programmed load changes in order to mark successive positions of the crack fronts.

Instead, the typical crack path in the ground and peened specimens was traced by stopping selected tests at different stages after crack initiation, and figure 5 is a schematic representation of the crack propagation pattern. Firstly, the crack initiates at the root and propagates upward to the surface of the weld. Thereafter, the crack propagates, on two separate fronts, downwards from the welds on the side of the balance pad, into the load bearing plate.

In order to calibrate the crack measuring systems used in this work (and to estimate crack growth rates), it was necessary to mark the crack front at various stages during propagation in the tests on the as-welded specimens. In the initial tests [3] this was done by heat tinting the specimen at three or four stages during the propagation of the crack. The specimens were subsequently beach-marked, by changing the test conditions, rather than heat-tinted. As will be outlined later, the technique, although yielding useful information, also affected the crack growth rates. It will be appreciated that, in order to produce a distinct series of beachmarks, the applied stress conditions have to be altered substantially. Thus, when changing from a high stress range to a low stress range, there was some crack retardation. However, for the purposes of this particular investigation, the (relatively small) overload retardation effects on crack growth rates do not have a significant influence on the overall results.

Figure 6(a) shows the data obtained in this test programme for the change in crack depth (a) with surface length (2c). A straight line was best-fitted to this data with a regression coefficient of 0,99. However, from this figure it is apparent that estimating the crack length for a crack depth of 7,5 mm (for example) could give an error of approximately 20 mm. Additionally, there is little data for small crack depths, and the best fit straight line does not pass through the origin. Figure 6(b) shows the change in crack aspect ratio (a/2c), in relation to the change in fractional crack depth (a/t). This graph does not show the same linear dependence as figure 6(a), but it should be noted that the crack shape during the initial stages of propagation (low a/2c or low a/t, or both) is strongly dependent on the initiating flaw. However, for a/t greater than about 0,5, the scatter is much reduced, as indicated by the lines enveloping the data in figure 6(b). This dependence of the early crack shapes on the initiating flaw also accounts for the fact that the best fit line in figure 6(a) does not pass through the origin.

It has been observed by a number of workers [5, 9-14] that fatigue cracks will tend to an equilibrium shape during propagation. This effect was investigated in several materials [9], and it was shown that although the initial growth pattern of the fatigue cracks were defined by the initiating notch, the growth curves then tended to join a common curve, as shown in figure 7. Thus it is to be expected that, for the welded samples under investigation here, the preferred crack propagation paths will be different, due to the differing initiating notch shapes.

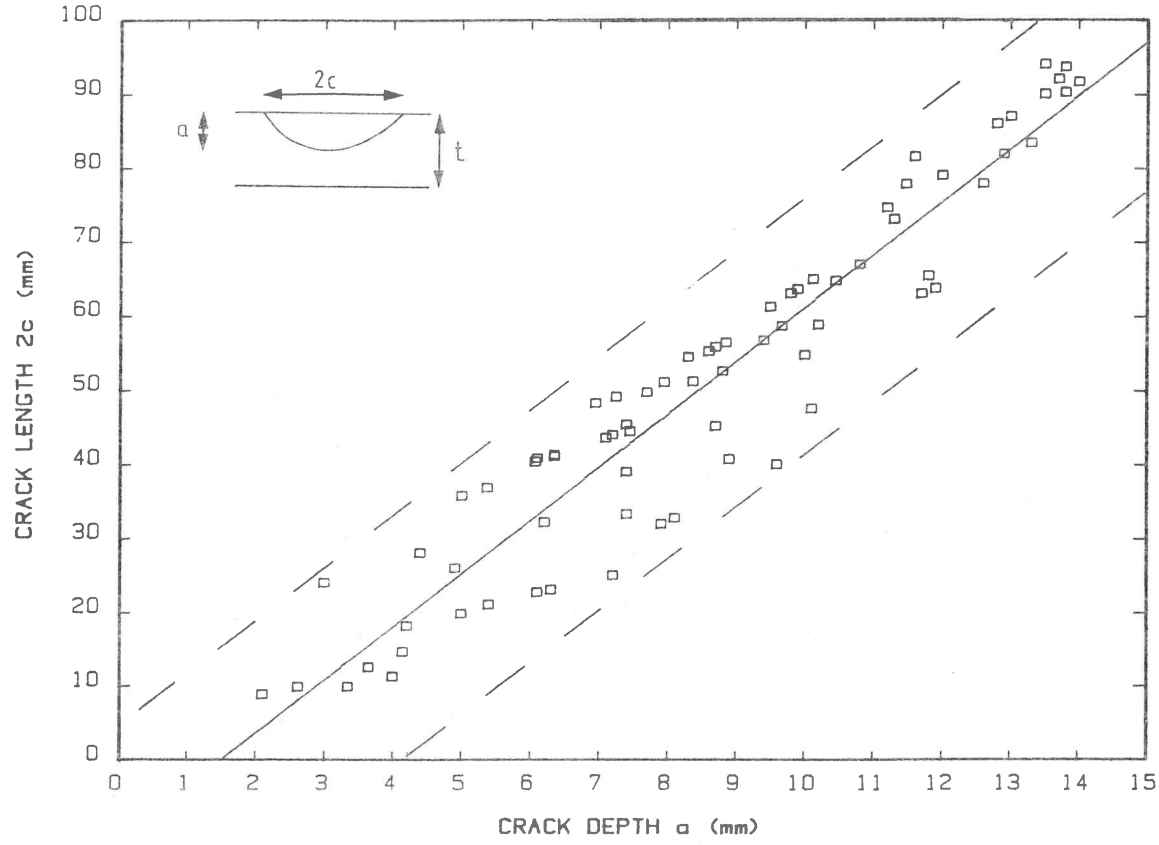

Figure 6 –
(a) The experimental results obtained for the change in crack depth (a) with surface length (2c)

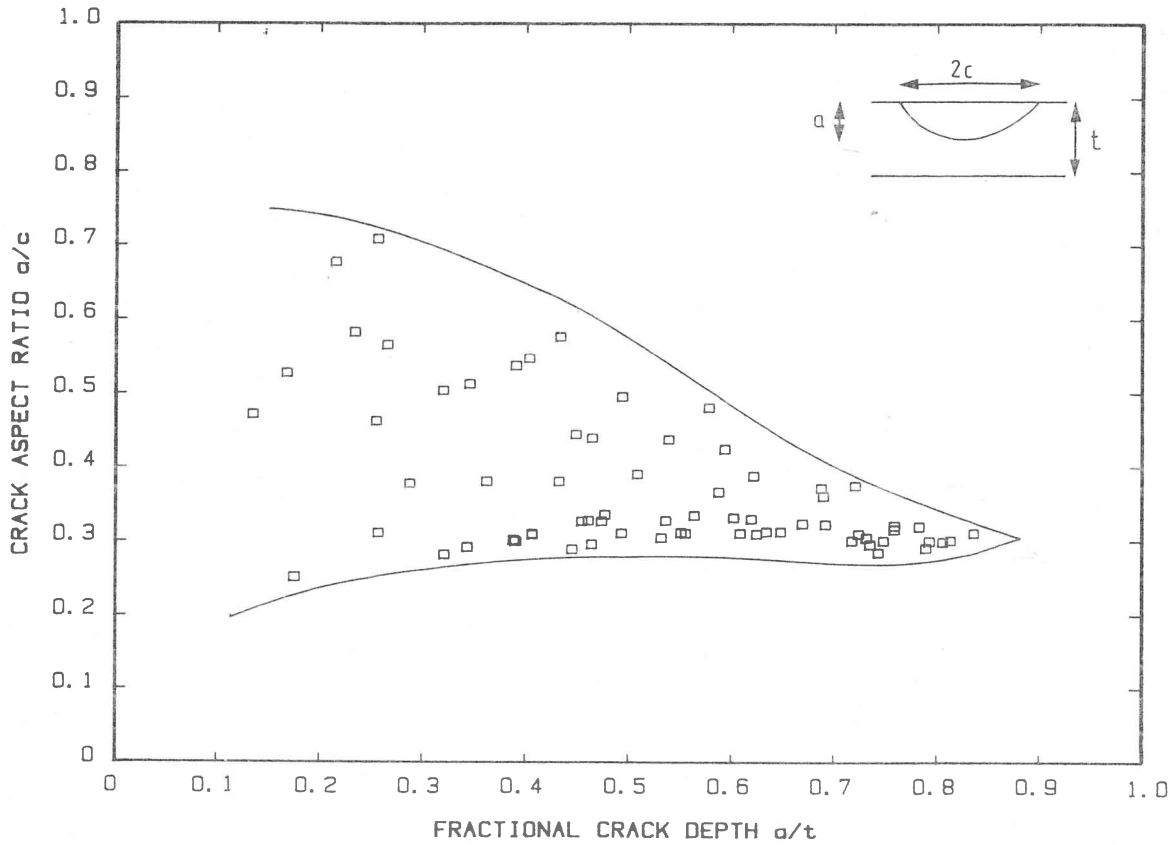

Figure 6 –
(b) The experimental results obtained for the change in crack aspect ration with fractional crack depth

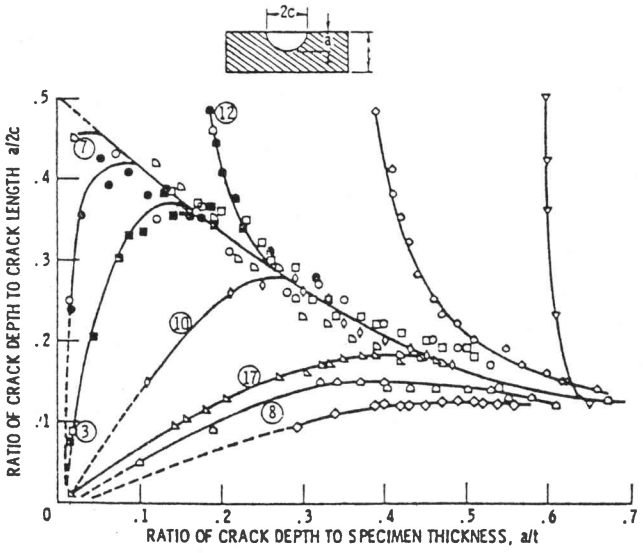

Figure 7 – A graphical representation of the influence of the initial notch shape on the crack growth development, the numbers 3, 8, 10 and 17 indicate starter notches with a small aspect ratio; 7 and 12 indicate starter notches with a large aspect ratio (From [9])

Crack growth rates

The potential drop was monitored throughout each test, and gave an indication of crack initiation, as well as the position and the relative extent of the crack. The change in voltage, as measured for the continuous, undressed weld specimens, is plotted against the crack depth in figure 8. It will be noted that there is some scatter in these results, arising principally from the fact that it is virtually impossible, even with a template, to have reproducible *electrical* spacings [10]. This is due to the nature of the specimens, and the fact that the crack initiation site is at the toe of the weld. The specimen surfaces are not smooth, and even if reproducible probe spacing is achieved, one of the probes must be attached to the weld as shown in figure 9. Thus, the electrical spacing (which depends on the actual surface distance between the contacts) will not necessarily be the same for two probe pairs. In addition, if one pair of p.d. probes did not straddle the initiation point, the potential drop did not change immediately upon initiation. However, the data presented in figure 8 does indicate that, for cracks deeper than about 3 mm, the change in the potential can be used to monitor the crack growth rate, although exact measurements of crack growth rate are not possible.

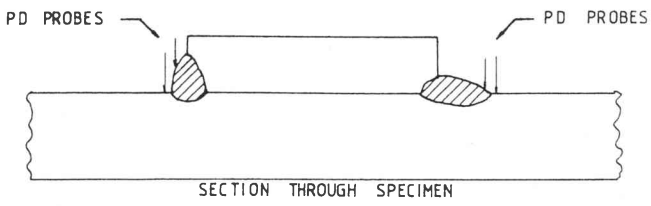

Figure 9 – A schematic illustration of the potential drop probe positions at the weld toe, showing that reproducible electrical spacing cannot be achieved (from [10]), note that the weld shape has been exaggerated for clarity

Initially [3] it was envisaged that the change in operating frequency of the resonant fatigue test facility could be used to mon-

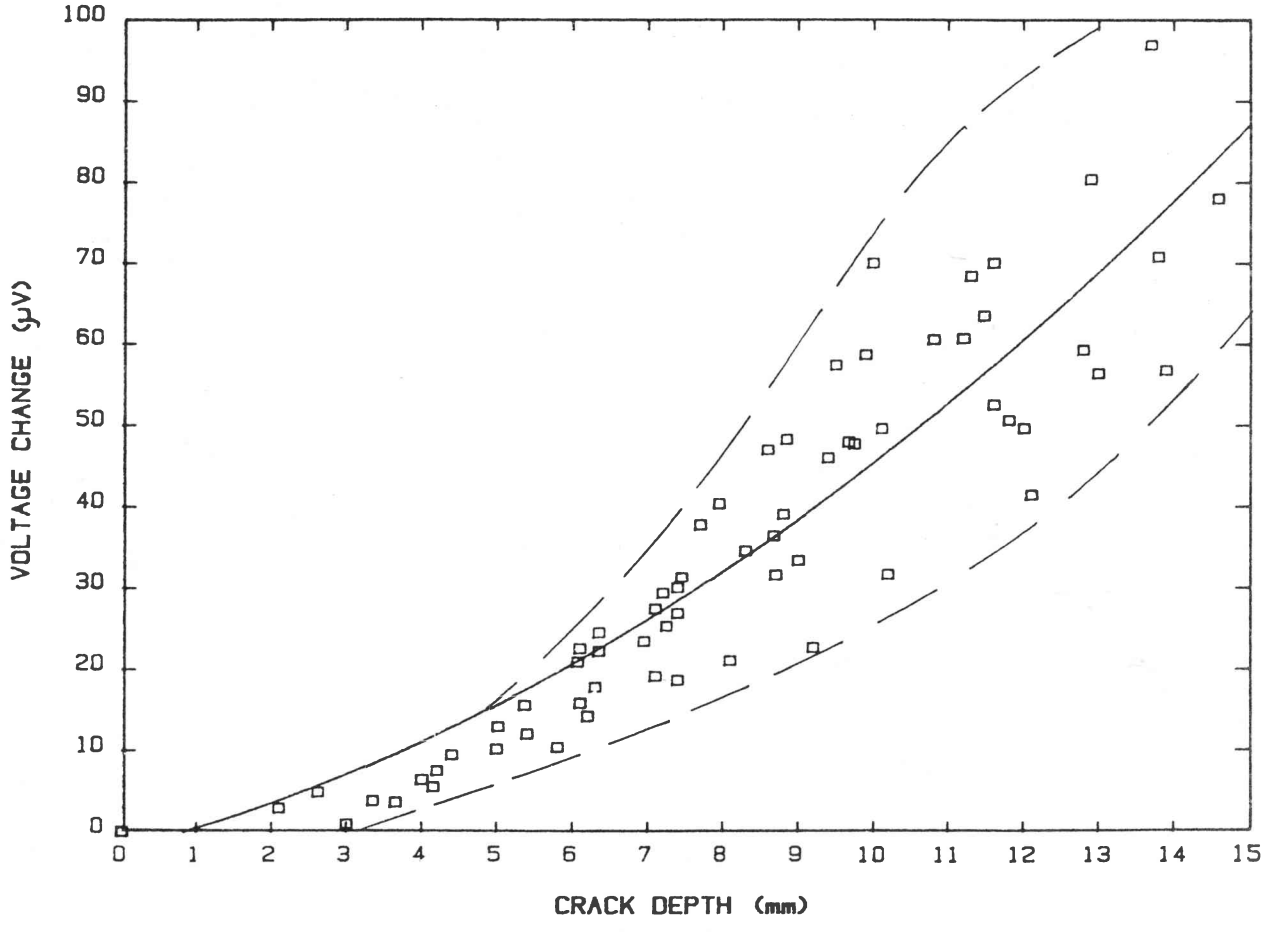

Figure 8 – The experimental results for change in potential drop with crack depth

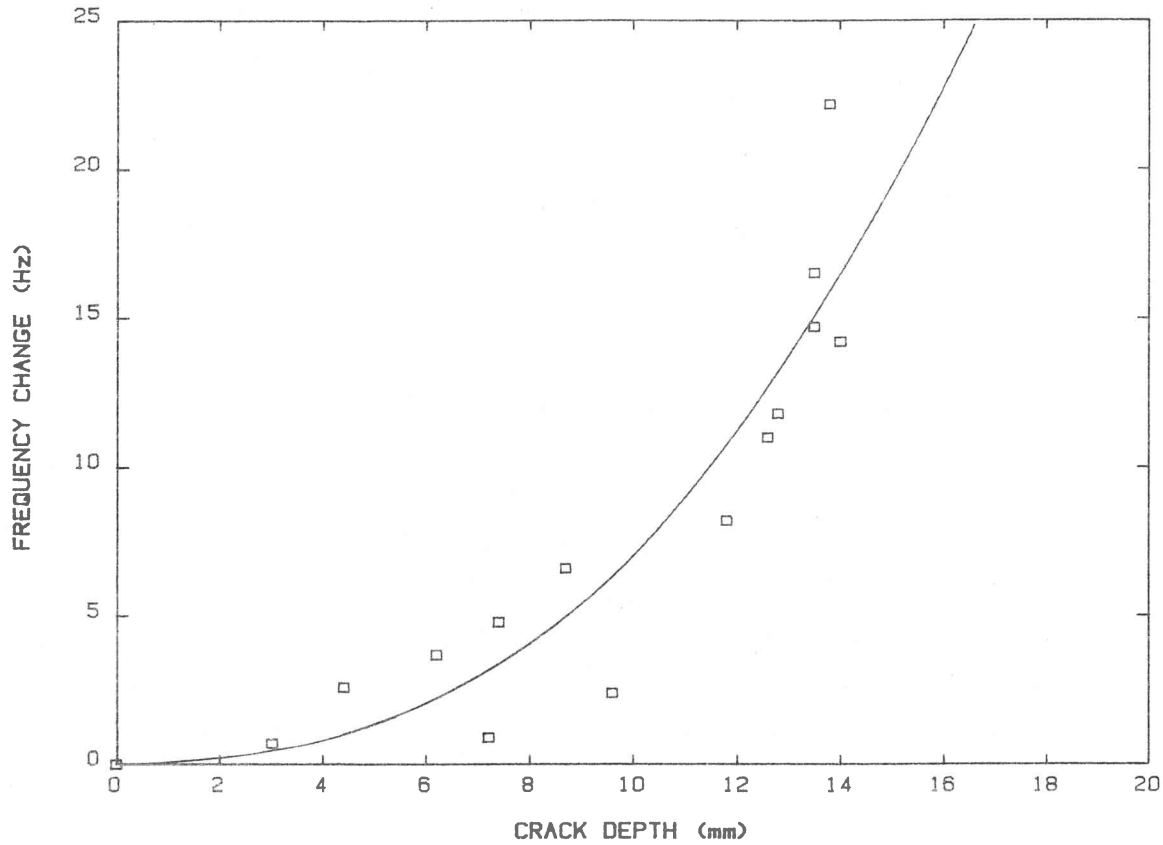

Figure 10 –
(a) The results obtained in correlating frequency change with crack surface area (heat-tinted specimens)

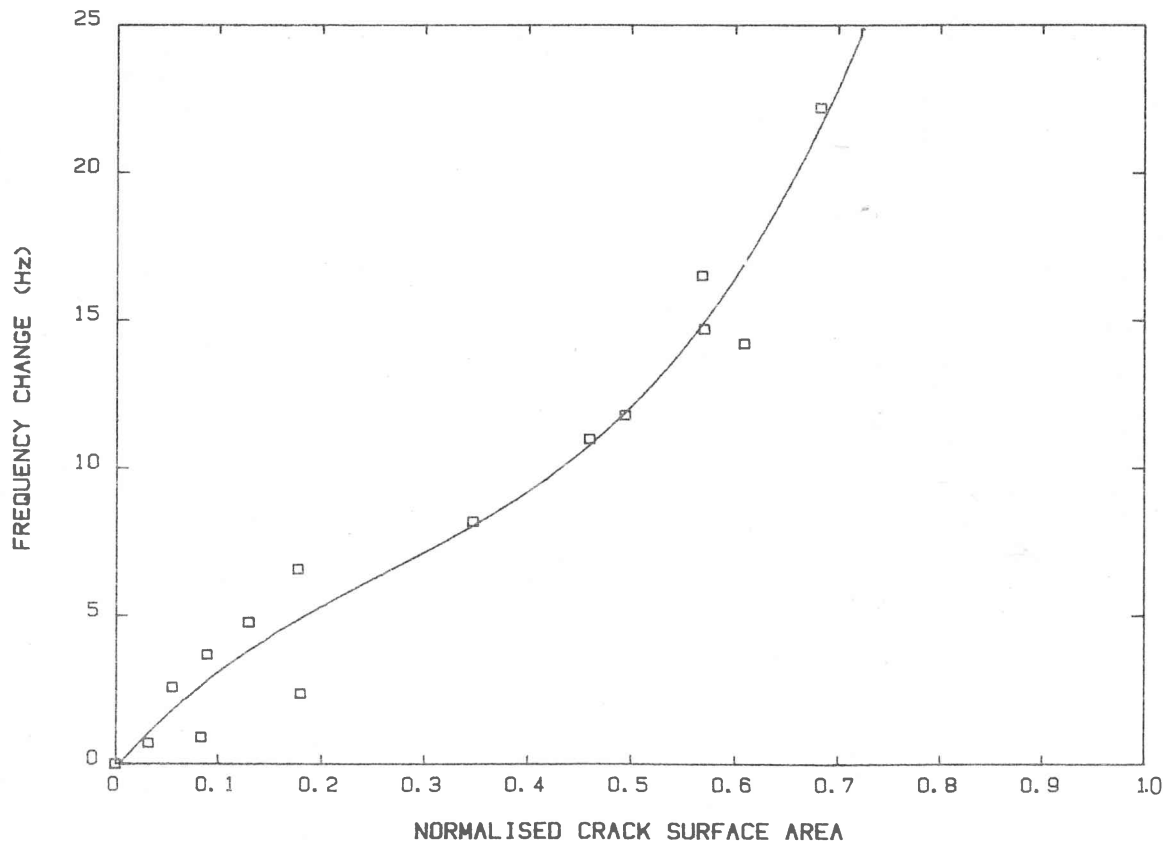

Figure 10 –
(b) The experimental correlation between frequency change and crack depth

itor crack growth. Again however, the method of marking successive crack fronts affected these results, since a change in operating stresses inevitably changed the operating frequency (before any further crack advance occurred). The results that were obtained for the heat-tinted specimens are shown in figure 10, and it will be noted that the change in frequency is plotted against the normalised crack surface area (figure 10(a)), and against the change in crack depth (figure 10(b)). This was done since the frequency change is affected by the increase in specimen compliance, and it was considered that this would be a function of the total uncracked area rather than the remaining ligament (or crack depth). Thus, the results shown in figure 10(a) were obtained by calculating the crack surface area, for each stage in the crack propagation, by assuming the crack shape to be semi-elliptical.

However, there is some considerable scatter in *both* these graphs, and this is ascribed to small errors in the crack depth and length measurements, and to the different initial crack shapes in the different specimens. In addition, the fact that the specimens were removed from the machine in order to be heat tinted would have caused some variation in the operating frequency of the resonant test facility. It is therefore clear that, in order to establish the exact correlation between frequency change and increasing crack depth or crack surface area, it will be necessary to devise some way of marking the crack front that does not entail changing the applied loading conditions, or removing the specimen from the machine. Such a correlation could possibly be achieved with a set of specimens that are identical, with identical preferred crack propagation paths, and stopping each test at a different stage after initiation. The different crack surface area (or crack depth) in each specimen could then be easily correlated with the observed change in frequency. Unfortunately, it is doubtful that such a correlation would be of much use in the fatigue testing of weldments!

Various solutions are available for the description of the stress intensity factor (K) for a surface crack in a plain plate specimen (defined here as K_p). These solutions [11, 12 and 13] have the general form:–

$$K_p = F(a/c)\ F(a/t)\ F(a/w)\ \sigma\sqrt{\pi a} \qquad (1)$$

where a is the crack depth, c the crack half-length, t is the plate thickness and w is the plate width. Thus, the accuracy with which the stress intensity at the crack tip can be calculated is dependent on accurate measurements of crack depth and length, which define the various correction factors F(a/c), F(a/t) and F(a/w).

However, these solutions obviously cannot be applied to welded specimens, because of the additional stress concentrating effect of the weld, which will have a significant effect on the early growth of the crack. Clearly, in order to fully assess the fatigue life of weldments, it is important to evaluate the stress concentration and the stress distribution at the weld toe. Thus finite element analyses have been performed [14-16] on specimen weldments in order to establish the magnification factor, M_k such that the stress intensity of a surface crack, initiating from a weld (K_w) may be evaluated:

$$K_w = M_k\ K_p \qquad (2)$$

The stress intensity solution proposed by the (UK) Welding Institute [14-16] was used in this test programme, and has the general form:–

$$K_w = M_k \frac{M_s M_t M_p}{O_o}\ \sigma\sqrt{\pi a} \qquad (3)$$

In equation (3), M_k is the correction for the stress concentrating effect of the weld toe, M_s is a correction factor to allow for the effect of a free surface at the crack mouth, M_t is a correction factor to allow for the presence of a free surface ahead of the crack (or a finite thickness correction), and M_p is a correction factor to allow for the crack tip plasticity, and is dependent on the plastic zone size. (These factors have been given the symbol M to signify that they are magnification factors). However, M_p will be small for fatigue crack propagation under nominally elastic stresses, and therefore can be ignored in most fatigue situations [14].

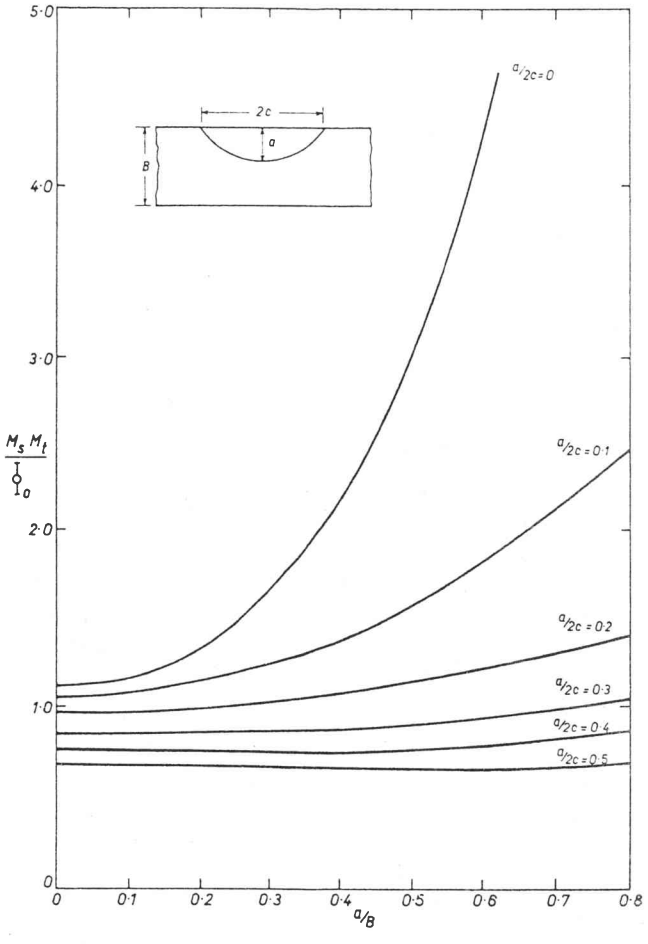

Figure 11 – Variation of the magnification factor with crack depth for various surface crack shapes (from [14])

O_o is the complete elliptical integral of the first kind, more often designated E_k, and specific values of this parameter can be obtained from standard tables [17], provided that the crack depth (a) and the crack length (c) are know. However, the Welding Institute method is to treat M_s, M_t and O_o as a single overall magnification factor, and values of this may be obtained directly from a graphical solution [14], reproduced here as figure 11. It can be seen that in order to evaluate this magnification factor, it is necesary to have accurate values for crack depth and length.

The original analysis [14] of M_k was subsequently revised in order that it would cater for a wider range of weld sizes and plate thicknesses [15, 16]; however, all these analyses predicted that the magnitude of M_k decreases rapidly with increasing crack depth. This is consistent with its definition, since this factor is the difference in stress intensity for a surface crack in a plain specimen compared to that in a welded specimen, as indicated in equation (2). Thus, as the distance of the crack tip from the weld increases, the stress concentrating effect of the weld is reduced.

Crack tip stress intensities and the corresponding rate of change in crack depth were calculated for the specimens in which the crack fronts were beach marked, and the results are shown in figure 12. There does appear to be some scatter in these results, but it must be indicated that, at these low crack growth rates (less than 10^{-8} m/cycle), any error in measuring the crack depths will be magnified on such a plot. Additionally, the method used to mark the successive crack fronts would give rise to some scatter in the crack growth rates, since to produce a dis-

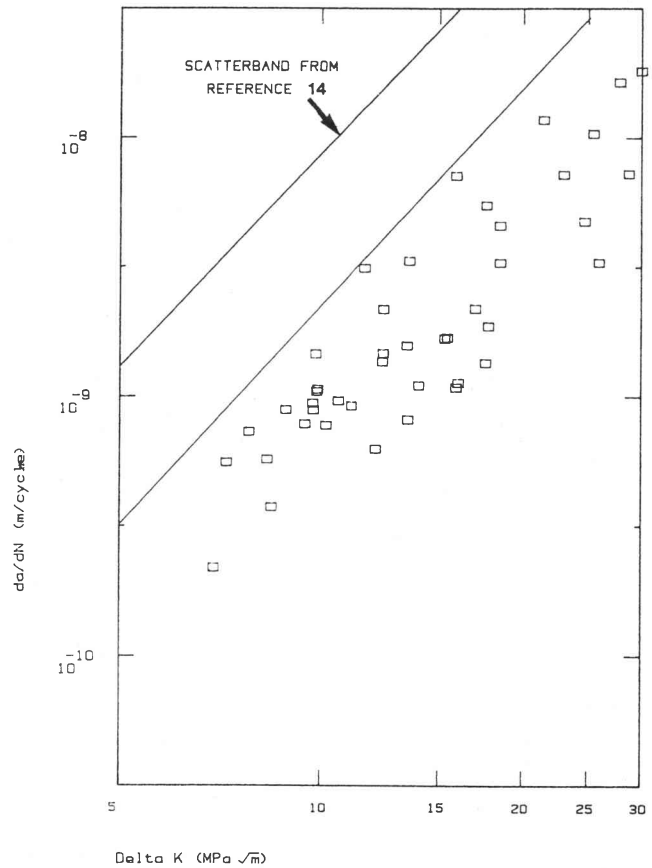

Figure 12 – da/dN versus ΔK for beachmarked specimens, these crack tip stress intensities were calculated from [14]

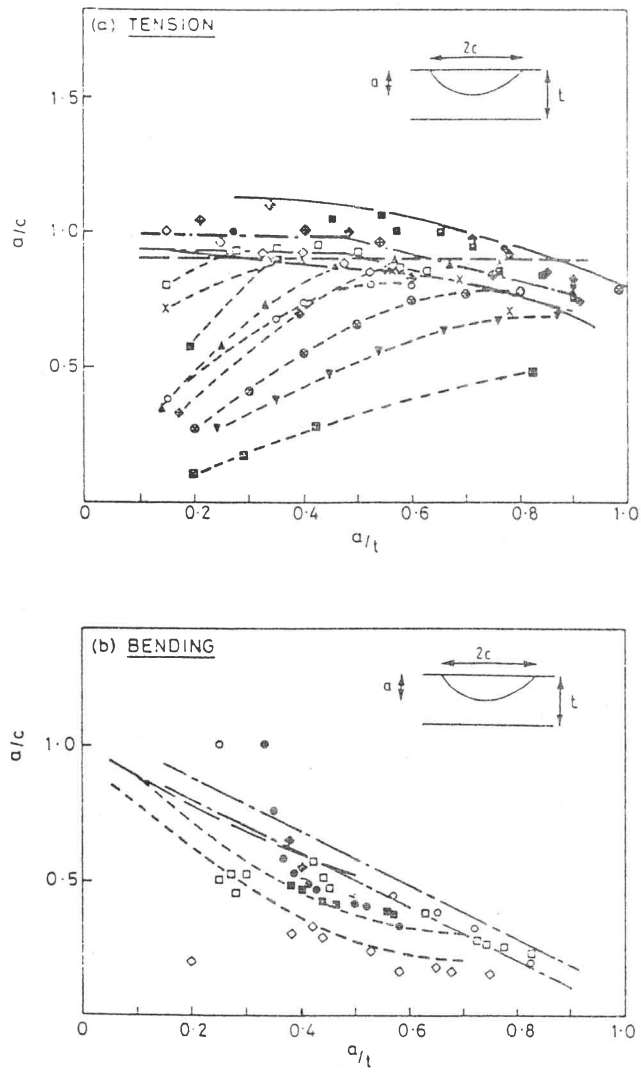

Figure 13 – The development of crack shape under (a) direct tension and (b) pure bending, the different symbols refer to various data sources [13]

tinct beach mark, it was found necessary to either double or halve the previous stress range. Thus, there could be some crack retardation when changing from a high stress range to a low stress range.

It can also be seen that the results obtained in this test programme lie outside of the scatterband for cruciform joint specimens, tested in air to validate the proposed stress intensity solution [14]. This is due to the fact that the tests reported here were carried out under four-point bending, whereas the Welding Institute performed their tests under direct tension. It will be recalled from equation (3) that the stress intensity is evaluated from both the crack depth, a, and the surface length, 2c. It will further be recalled that the fatigue crack shape is dependent on the loading arrangement, and therefore the equilibrium shape adopted under bending is different to that due to tensile loading. Indeed, as shown in figure 13(a), under tensile loads the crack aspect ratio (a/c) tends to 1,0 as the fractional crack depth (a/t) increases, whereas the aspect ratio of a crack under bending loads (figure 8(b)) tends to 0 as the fractional crack depth increases. Although this is not expected to invalidate the stress intensity factor calculation, it will cause a variability between the stress intensity for the two cases of tension and bending for a given crack depth and applied stress, since this is uniquely defined by the specific values of a *and* 2c. Moreover, the rate of change of crack depth (da/dN), at a given crack depth, will be different for the two cases.

The method used for calculating stress intensities in fillet welded specimens [14-16] only evaluates the conditions at the deepest part of the crack. Solutions have been published [13] for the stress intensity at the surface, but these are only valid for plain plate specimens. Thus, the rate of change of surface length (d2c/dN) obtained in the present study was plotted against the corresponding rates of change of crack depth (da/dN) in figure 14, and it can be seen that the rate of change of surface length is an order of magnitude greater than the rate of change of crack depth. This is consistent with the semi-elliptical shapes developed in these specimens.

It was initially intended that the crack shape development data (i.e. a/2c versus a/t or a versus 2c) would be used, in conjunction with the change of potential drop with crack depth, to estimate crack depths and crack lengths continuously during propagation. The crack tip stress intensity would then be calculated for these small increments of growth (e.g. every μV change in potential), and this would yield a continuous da/dN versus K for a particular test, without changing the stress conditions to mark the crack front.

However, as seen in figures 6 and 8, there was some considerable scatter in the experimental correlations. In order to evaluate the effect of this scatter on the proposed method of monitoring the crack growth and continuously calculating the crack tip stress intensities, three potential drop readings obtained during the testing of one particular specimen were used to extrapolate for values of crack depth, from figure 8. For each potential drop reading, three crack depths were obtained, corresponding to the mean regression value, and the two outer limits of the experimental scatterband. For each of these three crack depths, three surface lengths were obtained from the experimental data shown in figure 6(a), and the stress intensity of each of the nine

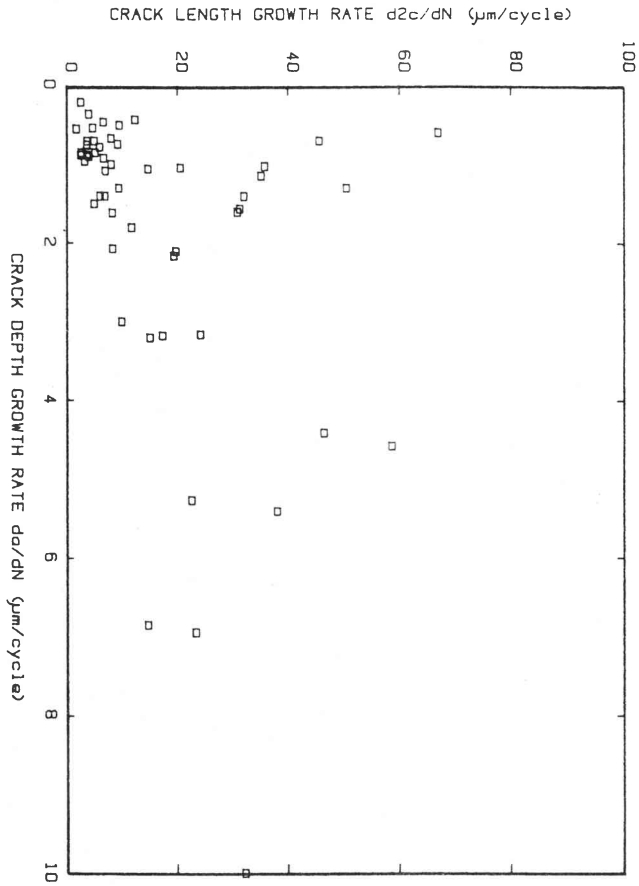

Figure 14 – The results obtained for the rate of change of crack depth (da/dN) compared with the rate of change of crack surface length (d2c/dN)

possible defect shapes were evaluated. Thus, for each potential drop reading, three predicted values of crack growth rate (da/dN) were calculated, and for each of these three growth rates, three cyclic stress intensities ($\triangle K$) were evaluated. In addition, of course, the "true" da/dN and $\triangle K$ were evaluated from the beachmarked fracture surface. The results of this excercise, shown in figure 15, indicate that the scatter observed in the correlation of potential drop with crack depth, and of crack depth with crack length give significant errors in the evaluation of the crack tip stress intensity. In figure 15 the three sets of data are represented by different symbols, and for further clarity, the "true" data point of each set is represented by a solid symbol.

However, the results obtained in the evaluation of da/dN and $\triangle K$ from the beachmarked specimens gave sufficient information for the purposes of evaluating crack growth rates, in this particular investigation. Indeed, all the results described in this paper were of considerable value in the investigation of the fatigue behaviour of various fillet weld details. This experimental test programme was aimed at establishing the 10 million cycle endurance limit of non-load-carrying fillet welds, and evaluating the effects of weld procedure and post-weld dressing techniques on this endurance limit. The identification of the crack initiation sites indicated the need for weld dressing procedures to be implemented, such that the weld toe profile was modified, and the preferential crack initiation site was either removed or placed in a state of compressive residual stress. This resulted in fatigue cracks initiating at higher applied stress levels, remote from the weld toe. Identification of the crack initiation site in the dressed specimens served to indicate whether or not the dressing had been effectively carried out. The evaluation of the crack shape development was essential in the calculation of crack growth rates and crack tip stress intensity factors. Thus, these macroscopic features could also be used, in a qualitative manner, in the investigation of service fatigue failures.

Summary

This paper has reviewed the features observed in the macroscopic examination of the fatique fracture surfaces of the specimen weldments. These features were used to substantiate the results obtained in the investigation of the fatigue behaviour of non-load-carrying fillet welds, described in a companion paper [6].

It was shown that initiation typically occurs subsurface, at the root of the weld, in the stitch welded samples although there were some instances of crack initiation from the weld ends.

The presence of weld toe undercut in the continuous specimens causes a drastic reduction in the fatigue strength of this weld detail. In the absence of undercut, multiple initiation occurs from the weld toe, and this required much higher stress ranges. If these preferential crack initiation sites are removed by post-weld mechanical dressing, the crack initiation site is removed from the weld toe to the weld root with a corresponding increase in the fatigue strength. However, initiation can occur from the weld toe if defects remain there after the grinding or peening, indicating that some care is needed for the successful implementation of these improvement techniques. On the other hand, initiation can occur from the flame cut edge of the main load bearing plate, remote from the dressed welds.

Heat-tinting and beachmarking techniques were used to locate the successive positions of the crack front during propagation. It was shown that the shape of the cracks developed in the

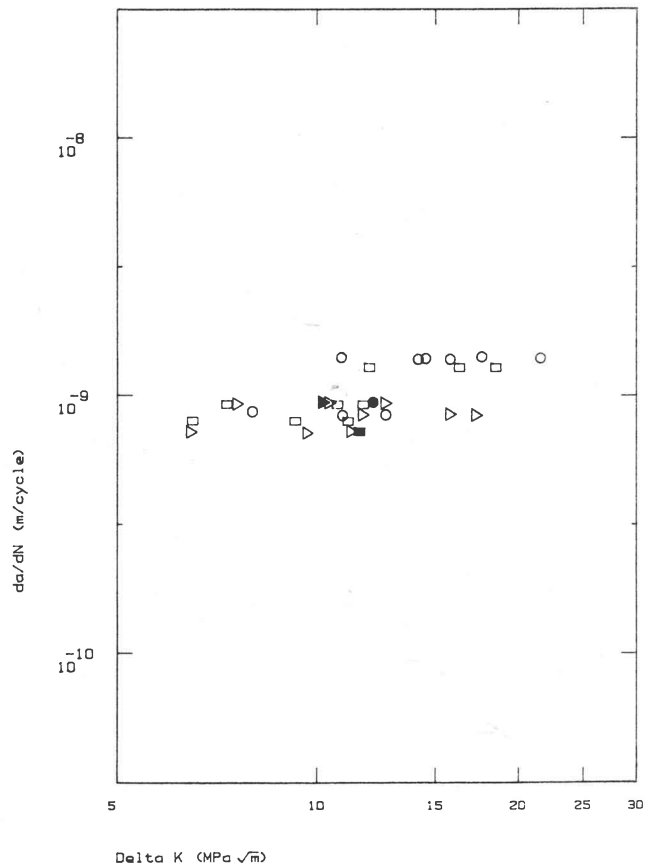

Figure 15 – The results obtained in predicting crack tip stress intensities from the experimental correlations between crack depth and potential drop, and between crack depth and crack length, each symbol type represents one potential drop reading, the open symbols are calculated from the predicted crack parameters, the solid symbols are the actual results calculated from the beachmarks

as-welded specimens is subject to some variability due to the different initiating defect shapes. However, the cracks tended to the semi-elliptical equilibrium shape expected for this geometry and loading arrangement. In the ground and peened specimens, on the other hand, multiple crack propagation occurs and this particular growth pattern was established by stopping selected specimens at different stages after initiation had occurred.

Both the potential drop and the compliance methods were evaluated for use as crack monitoring techniques. However, it was necessary to mark the crack front during propagation in order to calibrate these methods, and this affected the correlation between specimen compliance and crack depth. The potential drop technique is inherently inaccurate for this specimen geometry, especially during the initial growth stages. Thus, it was not possible to use the potential drop, or the compliance method to evaluate crack growth rates and crack tip stress intensities continuously during testing.

However, the results from the beach-marked specimens indicated that the cyclic stress intensity at the crack tip (at the deepest point of the crack front) ranged between 5 and 30 MPa$\sqrt{m}$, depending on the crack depth and applied stress level, and this corresponded to rates of change of crack depth of between 3×10^{-10} and 7×10^{-9} m/cycle.

Finally, it was shown that the rate of change of crack length was an order of magnitude faster than the rate of change of crack depth; this is consistent with the semi-elliptical equilibrium crack shape.

Acknowledgements

This work was performed under the auspices of the Fracture Research Group at the University of the Witwatersrand, and was primarily sponsored by ESKOM and Airtec Davidson. One of the authors, dr. C. A. Boothroyd, received additional financial support in the form of University and CSIR post-graduate bursaries. Laboratory facilities were provided by the Department of Metallurgy and Materials Engineering, and all samples were supplied by Airtec Davidson.

References

1. Dahlgren, C. A., Tait, R. B., Franco, S., Spencer, D. P., Patton, R. G., and Garrett, G. G., "Fatigue Failure of a Large Industrial Fan." Fracture and Fracture Mechanics – Case Studies, Proc. 2nd National Conference of Fracture, Johannesburg. Eds: R. B. Tait and G. G. Garrett, Pergammon Press, Oxford, 1985. pp. 137-146.

2. Gurney, T. R., "Fatigue design rules for welded steel joints." The Welding Institute Research Bulletin, May 1976. pp. 115-124.

3. Boothroyd C. A. and Garrett G. G., "Fatigue cracking from non-load carrying fillet welds at low growth rates." Department of Metallurgy, University of the Witwatersrand, Research Report FRP/85/12, March 1985.

4. Gurney T. R., "Fatigue strength of beams with stiffeners welded to the tension flange." Br. Weld. J., 7 (3), 1960, pp. 569-576.

5. Smith I. F. C. and Smith R. A., "Defects and crack shape development in fillet welded components." *Fat. Eng. Matls. and Struct.* Vol 5, No 2, 1982, pp. 151-165.

6. Boothroyd C. A. and Garrett G. G., "The fatigue strength of non-load-carrying fillet welds." *R and D Journal*, April 1988.

7. Kriel Site Investigation, Davidson Research Centre, Job No. SA 83/32, November 1983.

8. Gurney, T. R., "Fatigue of welded structures." Second Edition, Cambridge University Press, Cambridge, 1976. pp. 80-81.

9. Pierce W. S. and Shannon J. L., Jr. "Surface-crack shape change in bending fatigue using an inexpensive resonant fatigue apparatus." *JTEVA*, Vol. 6, No. 3, May 1978, pp. 183-188.

10. Smith I. F. C. and Smith R. A., "Measuring fatigue cracks in fillet welded joints." *Int. J. Fatigue*, January 1982, pp. 41-45.

11. Burck L. H., "Fatigue crack growth of surface cracks in bending." *Eng. Frac. Mech.* Vol. 9, 1977, pp. 389-395.

12. Scott P. M. and Thorpe T. W., "A critical review of crack tip stress intensity factors for semi-elliptical cracks." *Fat. of Eng., Mat. and Struct.* Vol. 4, No. 4, 1981, pp. 291-309.

13. Holdbrook S. J. and Dover W. D., "The stress intensity factor for a deep surface crack in a finite plate." *Eng. Frac. Mech.* Vol. 12, 1979, pp. 347-364.

14. Maddox S. J., "An analysis of fatigue cracks in fillet welded joints." *Welding Institute Research Report* 32/1977/E. The Welding Institute, March 1977.

15. Gurney T. R., "Theoretical analysis of the influence of toe defects on the fatigue strength of fillet welded joints." *Welding Institute Research Report* 32/1977/E, The Welding Institute, March 1977.

16. Gurney T. R. and Johnston G. O., "A revised analysis of the influence of toe defects on the fatigue strength of transverse non-load-carrying fillet welds." *Welding Institute Research Report* 62/1978/E, The Welding Institute, April 1978.

17. Pierce B. O., "A short table of integrals." 4th Edition. (Revised by P. M. Foster), Ginn and Company, 1957, pp. 133-135.